



 Cite this: *RSC Adv.*, 2021, 11, 22250

# Solvothermal synthesis of octahedral and magnetic CoFe<sub>2</sub>O<sub>4</sub>–reduced graphene oxide hybrids and their photo-Fenton-like behavior under visible-light irradiation†

 Liling Hu,<sup>ab</sup> Meng Li,<sup>a</sup> Lihong Cheng,<sup>a</sup> Bofan Jiang<sup>a</sup> and Jianping Ai <sup>\*a</sup>

We report a facile solvothermal synthesis of novel octahedral CoFe<sub>2</sub>O<sub>4</sub>–reduced graphene oxide (RGO) hybrid and pure CoFe<sub>2</sub>O<sub>4</sub> that were used as heterogeneous photo-Fenton catalysts for the degradation of organic dyes in water. We investigated the structures, morphologies and catalytic activity of both the CoFe<sub>2</sub>O<sub>4</sub> nanoparticles and CoFe<sub>2</sub>O<sub>4</sub>–RGO hybrids. The morphology of CoFe<sub>2</sub>O<sub>4</sub> nanoparticles displays size-dependent shapes changing from granular (or sheet) to octahedral shapes with the introduction of RGO. Compared with bare CoFe<sub>2</sub>O<sub>4</sub>, the octahedral CoFe<sub>2</sub>O<sub>4</sub>–RGO hybrids serve as novel bifunctional materials displaying higher saturation magnetization values and excellent heterogeneous activation of H<sub>2</sub>O<sub>2</sub> at nearly neutral pH. The high saturation magnetization (41.98 emu g<sup>-1</sup>) of CoFe<sub>2</sub>O<sub>4</sub>–RGO hybrids aids their separation from the reaction mixture. In addition, the remarkable enhancement in the photo-Fenton activity of the CoFe<sub>2</sub>O<sub>4</sub>–RGO hybrids under visible light irradiation was attributed to the graphene/CoFe<sub>2</sub>O<sub>4</sub> heterojunction, which aided the separation of excited electrons and holes. Furthermore, the CoFe<sub>2</sub>O<sub>4</sub>–RGO hybrids exhibited better removal efficiency for cationic methylene blue (MB) dye than for anionic methyl orange (MO) dye. Meanwhile, the CoFe<sub>2</sub>O<sub>4</sub>–RGO hybrids displayed acceptable photocatalytic stability, and we proposed an activation mechanism of H<sub>2</sub>O<sub>2</sub> by the octahedral CoFe<sub>2</sub>O<sub>4</sub>–RGO hybrids.

Received 21st April 2021

Accepted 11th June 2021

DOI: 10.1039/d1ra03103a

[rsc.li/rsc-advances](https://rsc.li/rsc-advances)

## 1. Introduction

It is well-known that the inappropriate disposal of organic effluents from industries raises environmental concerns.<sup>1,2</sup> Among many methods used for the treatment of industrial effluents, graphene-based adsorption is a highly efficient and less time-consuming method owing to its exceptionally large surface area, open porous structure, and excellent chemical stability.<sup>3–5</sup> However, the separation and recycling of graphene used for purification of industrial wastewater remain a challenge, and this limits its further application.<sup>6</sup>

Nowadays, the integration of magnetic particle technology to solve water pollution problems has attracted the interest of many researchers.<sup>7,8</sup> Firstly, the dispersion of magnetic nanoparticles (NPs) on graphene sheets enables the development of materials with promising separability and reusability. This is because the graphene-based hybrids containing magnetic NPs do not introduce foreign pollutants into the wastewater system

during the whole purification process.<sup>9</sup> Furthermore, the magnetic NPs can enhance the functionalities of graphene-based hybrids; therefore, the potential of magnetic NPs–graphene hybrids is huge, and they can be widely applied in catalysis and water purification.<sup>10</sup> In view of these, several studies have been conducted to investigate the adsorption and photocatalytic performance of graphene-based hybrids containing magnetic NPs. Yao *et al.*<sup>11</sup> fabricated magnetic Fe<sub>3</sub>O<sub>4</sub>@graphene hybrids. The methylene blue (MB) and Congo red (CR) absorption capacities of these hybrids good and separation of the hybrids after absorption was easy. Fu *et al.* synthesized a set of graphene-based nanocomposite photocatalysts including MFe<sub>2</sub>O<sub>4</sub>–graphene (M = Zn, Ni, Mn, Co) hybrids. These photocatalysts show high visible-light-responsive photo-degradation efficiency towards dyes. They were also stable and the photocatalyst can be conveniently separated by the use of an external magnetic field.<sup>12–15</sup>

Among these magnetic NPs, cobalt ferrite (CoFe<sub>2</sub>O<sub>4</sub>) nanocrystals with a spinel structure have attracted a great deal of attention for environmental remediation owing to their outstanding properties, such as their size- and shape-dependent magnetic behavior, and their relatively lower bandgap that perfectly matches with the solar spectrum.<sup>16–18</sup> To date, several studies have been conducted using CoFe<sub>2</sub>O<sub>4</sub> as

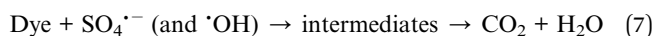
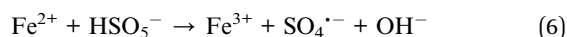
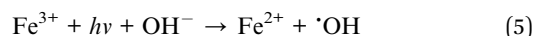
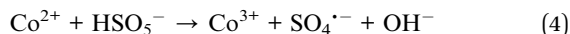
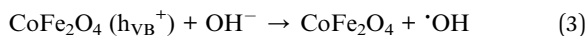
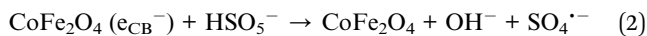
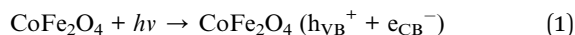
<sup>a</sup>Jiangxi Key Laboratory of Surface Engineering, Jiangxi Science & Technology Normal University, Nanchang 330013, P. R. China. E-mail: ai861027@163.com

<sup>b</sup>Dean of Students Office, Jiangxi Science & Technology Normal University, Nanchang 330013, P. R. China

† Electronic supplementary information (ESI) available. See DOI: 10.1039/d1ra03103a



heterogeneous catalysts for activating hydrogen peroxide<sup>19,20</sup> or peroxymonosulfate (PMS).<sup>21–23</sup> When heterogeneous PMS is activated for the degradation of dyes, the reaction mechanism is represented by the following equations:<sup>19,23–26</sup>



Interestingly,  $\text{CoFe}_2\text{O}_4$  possesses obscure Co leaching properties owing to its strong Fe–Co linkages. Moreover, Fe helps to enrich the hydroxyl group content on the surface of Fe–Co catalysts, and  $\text{CoFe}_2\text{O}_4$  are magnetically recyclable owing to the unique ferromagnetic properties. A number of studies have shown that when immobilization of  $\text{CoFe}_2\text{O}_4$  nanoparticles onto graphene sheets, the Fenton-like catalysis efficiency of the resultant hybrid catalyst improved remarkably. Moitra *et al.*<sup>20</sup> used  $\text{CoFe}_2\text{O}_4$ -reduced graphene oxide (RGO) nanocomposites for heterogeneously activating  $\text{H}_2\text{O}_2$ . The  $\text{CoFe}_2\text{O}_4$ -RGO exhibited good visible-light-responsive photocatalytic properties for the degradation of various synthetic dyes. Lu<sup>9</sup> and He<sup>27</sup> *et al.* have studied the effects of RGO contents, initial solution pH,  $\text{H}_2\text{O}_2$  concentration and operation parameters (*e.g.* dosage and dye concentration) on the catalytic activity. Their results showed that the incorporation of the graphene significantly enhanced the photocatalytic performance of the  $\text{CoFe}_2\text{O}_4$  in which the graphene acted as a charge carrier to capture the delocalized electrons. In addition, the  $\text{CoFe}_2\text{O}_4$ -graphene hybrids exhibited good reusability and were easily separated from the reaction mixture. To the best of our knowledge, the effect of particle size and shape of  $\text{CoFe}_2\text{O}_4$  on catalytic activity and magnetic properties of  $\text{CoFe}_2\text{O}_4$ /graphene nanocomposites, has been rarely studied. Moreover, there are few reports on the relationship between the adsorption behavior and surface charge of  $\text{CoFe}_2\text{O}_4$ /graphene nanocomposites. Furthermore, very few reports about the underlying growth mechanism of octahedral  $\text{CoFe}_2\text{O}_4$  on graphene sheets are available.

In the present study, we synthesized octahedral  $\text{CoFe}_2\text{O}_4$ -RGO hybrids *via* interface engineering. These hybrids served as excellent heterogeneous catalysts for activating  $\text{H}_2\text{O}_2$  at nearly neutral pH. In addition, the catalytic performance of  $\text{CoFe}_2\text{O}_4$ -RGO hybrids was evaluated for the degradation of diverse dyes, *i.e.* MB and methyl orange (MO), under visible-light irradiation. Also, we have presented the underlying photo-Fenton-like behavior and have investigated the remarkable effect of particle size and shape of  $\text{CoFe}_2\text{O}_4$  NPs in  $\text{CoFe}_2\text{O}_4$ -RGO hybrids to promote the Fenton chemistry and tuning of the magnetic property.

## 2. Experimental

### 2.1. Chemicals and reagents

Cobaltous nitrate hexahydrate ( $\text{Co}(\text{NO}_3)_2 \cdot 6\text{H}_2\text{O}$ , 99%), ferric nitrate nonahydrate ( $\text{Fe}(\text{NO}_3)_3 \cdot 9\text{H}_2\text{O}$ , 99.9%), isopropanol (IPA, AR), methylene blue (MB, AR), and methyl orange (MO, AR) were obtained from Sinopharm chemical reagent Co., Ltd (Shanghai, China). Hydrogen peroxide ( $\text{H}_2\text{O}_2$ , 30%), ethanol, and sodium hydroxide (NaOH, AR) were purchased from Xilong Chemical Co., Ltd (Shantou, China). A graphene suspension (thickness,  $\sim 0.8$  nm;  $1$  mg  $\text{mL}^{-1}$ ) was supplied by XFNANO Materials Tech Co. Ltd (Nanjing, China). Deionized water was supplied by a Milli-Q ultrafiltration system (Billerica, USA).

### 2.2. Synthesis of materials

The reduced graphene oxide loading in the  $\text{CoFe}_2\text{O}_4$ -RGO hybrids was adjusted by changing the initial volume ( $x$ ) of graphene suspension. And the sample was denoted as  $\text{CoFe}_2\text{O}_4$ -RGO( $x$ ) (where  $x = 35$  and  $70$  mL). As a typical procedure,  $35$  mL of the graphene suspension was dissolved in  $265$  mL of ethanol while it constantly stirred using a magnetic stirrer, and it was then sonicated for  $30$  min. Secondly,  $4.3654$  g of cobaltous nitrate hexahydrate and  $12.1164$  g of ferric nitrate nonahydrate were directly added to the above graphene solution while it was vigorously stirred for  $30$  min. The concentration of  $\text{Co}^{2+}$  and  $\text{Fe}^{3+}$  in the resulting solution (marked as solution A) was  $0.05$  mol  $\text{L}^{-1}$  and  $0.1$  mol  $\text{L}^{-1}$ , respectively. Subsequently, a  $4$  M NaOH solution was added dropwise to a uniform solution A until a pH of  $\sim 13$  was attained, and this resulted in complete precipitation of the metal cations. The resultant mixture was then transferred into four Teflon-lined stainless-steel autoclaves (volume:  $100$  mL, degree of filling:  $\sim 80\%$ ), and heated in an oven at  $180$  °C for  $20$  h. The sample was allowed to naturally cool down to room temperature. The products were centrifuged and directly collected, then they were severally washed with deionized water and ethanol and dried at  $60$  °C for  $24$  h. For comparison, pure  $\text{CoFe}_2\text{O}_4$  NPs were also fabricated following a similar solvothermal process without the introduction of graphene.

### 2.3. Characterization

The X-ray diffraction (XRD) diffractograms were obtained using a D/Max-2550 diffractometer with Cu K $\alpha$  radiation source ( $\lambda = 0.15406$  nm). The Raman spectra were obtained using a HORIBA JY LabRAM HR evolution microspectrometer at an excitation wavelength of  $532$  nm. The Fourier transform infrared spectroscopy (FT-IR) spectra were recorded using a Spectrum Two FT-IR spectrophotometer with samples pressed in KBr. The exact amount of RGO in the as-obtained products was measured using a thermal gravimetric analyzer (TGA/DSC 3+, Mettler-toledo, Switzerland). The UV-visible diffuse reflectance spectra (DRS) were obtained using a UV-vis spectrophotometer (UV-2550, Shimadzu, Japan). The surface morphologies of products were observed using a scanning electron microscopy (GeminiSEM 500, Zeiss, Germany). The X-ray photoelectron spectroscopy (XPS) was carried out using a ThermoFisher

Scientific ESCALAB250Xi photoelectron spectrometer using with Al X-ray source. All binding energy values were calibrated using the carbon (C 1s) peak observed at 284.0 eV. The specific surface area and the pore-size distribution were measured using Autosorb-iQ2 (Quantachrome, USA) based on the nitrogen adsorption–desorption isotherms. The hysteresis loops were determined using a vibrating sample magnetometer (PPMS DynaCool Cryogen-free System 9 T, Quantum Design, USA). The zeta potential measurements were conducted on a zeta potential analyzer JS94K2 (Shanghai, China).

#### 2.4. Catalytic test procedure

The photocatalytic activities of the as-obtained samples were measured using the photocatalytic degradation of water-soluble dyes (MO or MB) under visible light irradiation together with H<sub>2</sub>O<sub>2</sub>. A 500 W xenon lamp (cut-off wavelength 420 nm) was used as the visible-light source in the photo-Fenton reaction. The distance between the surface of the reaction solution and the visible-light source was approximately 11 cm. The experiment was conducted as follows: 60 mg of the photocatalyst was dispersed into 60 mL of the 10 mg mL<sup>-1</sup> dye aqueous solution (MO or MB) while it was constantly stirred. Before irradiation, the solution was stirred using a magnetic stirrer in a dark room for 1.5 h to ensure the establishment of an adsorption/desorption equilibrium. Next, a certain amount of 30% H<sub>2</sub>O<sub>2</sub> was introduced into the above resultant mixture, which was then exposed to the visible-light source while the mixture was continuously stirred. The concentrations of MO and MB in the reacting mixtures were monitored by measuring the characteristic absorbance at wavelengths of 464 and 664 nm, respectively.

The removal rate (rev (%)) of the dyes (MO and MB) was determined using eqn (8):

$$\begin{aligned} \text{Removal rate (\%)} &= (A_0 - A_t)/A_0 \times 100\% \\ &= (C_0 - C_t)/C_0 \times 100\% \end{aligned} \quad (8)$$

where  $A_t$  is the absorbance of dye solution at  $t$  time,  $A_0$  is the initial absorbance of dye solution,  $C_0$  is the initial concentration of aqueous dye, and  $C_t$  represents the concentration of the aqueous dye at  $t$  time.

A trapping experiment, which is similar to the photo-degradation procedure, was conducted to identify the dominant reactive species upon the addition of 0.1 M IPA. Moreover, the photocatalytic stability of CoFe<sub>2</sub>O<sub>4</sub>-RGO hybrids was investigated *via* recycling tests. After each cycle, the catalyst was separated from the reaction solution using an external magnet, and it was washed several times with deionized water and ethanol. Then the same volume of fresh MB solution was added for the next cycle.

## 3. Results and discussion

### 3.1. Characterization and the synthesis mechanism

The XRD diffractograms of the bare CoFe<sub>2</sub>O<sub>4</sub> and CoFe<sub>2</sub>O<sub>4</sub>-RGO hybrids are shown in Fig. 1(a). The XRD diffractograms of CoFe<sub>2</sub>O<sub>4</sub>-RGO hybrids are identical to that of the bare CoFe<sub>2</sub>O<sub>4</sub>, which matches well with cubic spinel-type CoFe<sub>2</sub>O<sub>4</sub> (JCPDS 22-

1086).<sup>28</sup> Moreover, the observed diffraction peaks were sharp, implying that the as-prepared CoFe<sub>2</sub>O<sub>4</sub> particles were highly crystalline. Peaks attributed to impurities were not observed on the XRD diffractogram, indicating that the CoFe<sub>2</sub>O<sub>4</sub> samples were highly pure. In addition, the characteristic peak that was observed at  $2\theta = 26.5$  corresponding to RGO (002) was not detected in the XRD diffractogram of the CoFe<sub>2</sub>O<sub>4</sub>-RGO hybrids.<sup>29</sup> This may be ascribed to the proper separation and decoration of the RGO sheets by excess CoFe<sub>2</sub>O<sub>4</sub> nanoclusters, resulting in a low diffraction intensity of graphene in the XRD diffractogram of the CoFe<sub>2</sub>O<sub>4</sub>-RGO hybrids.

Fig. 1(b) shows the Raman spectra of bare CoFe<sub>2</sub>O<sub>4</sub> and the CoFe<sub>2</sub>O<sub>4</sub>-RGO hybrids. Three major Raman scattering peaks can be observed at about 312, 468, and 687 cm<sup>-1</sup>, which are attributed to the specific characteristics (A<sub>1g</sub>, E<sub>g</sub>, and 3T<sub>2g</sub>) of CoFe<sub>2</sub>O<sub>4</sub> ferrite.<sup>30</sup> CoFe<sub>2</sub>O<sub>4</sub>-RGO hybrids and pristine CoFe<sub>2</sub>O<sub>4</sub> show similar peaks in the range of 250 to 750 cm<sup>-1</sup>. In addition, the CoFe<sub>2</sub>O<sub>4</sub>-RGO hybrids exhibit two Raman peaks at approximately 1347 (D band) and 1589 cm<sup>-1</sup> (G band), where the D and G bands correspond to the RGO.<sup>17,31</sup> These results indicate that graphene has been incorporated into the CoFe<sub>2</sub>O<sub>4</sub>-RGO hybrids.

The hybridization of the CoFe<sub>2</sub>O<sub>4</sub> NPs with RGO was further verified by observing the FT-IR spectra (shown in Fig. 1(c)). For the CoFe<sub>2</sub>O<sub>4</sub> sample, the peaks at approximately 3446 cm<sup>-1</sup> and 1628 cm<sup>-1</sup> were respectively ascribed to the stretching and bending vibrations of O–H in the presence of water molecules adsorbed on the surface.<sup>29,32</sup> In addition, tetrahedral Co–O bonds were observed at approximately 593 cm<sup>-1</sup>, and the octahedral Fe–O stretching vibrations were observed at approximately 458 cm<sup>-1</sup>.<sup>16,21</sup> When compared with the bare CoFe<sub>2</sub>O<sub>4</sub>, some new peaks were observed in the CoFe<sub>2</sub>O<sub>4</sub>-RGO hybrids. The band at approximate 1630 cm<sup>-1</sup> may correspond to the C=C skeletal vibration of graphitic domains of RGO.<sup>33</sup> Furthermore, the peaks observed at 1398 and 1594 cm<sup>-1</sup> can be attributed to the deformation vibrations of the tertiary C–OH groups and the unoxidized carbon backbone on the surface of RGO, respectively.<sup>34–36</sup> Therefore, we can infer that the target CoFe<sub>2</sub>O<sub>4</sub>-RGO hybrids had been synthesized.

TG–DSC analysis was carried out under air atmosphere to confirm the amount of RGO present in the CoFe<sub>2</sub>O<sub>4</sub>-RGO hybrids (Fig. 1(d)–(f)). For pure CoFe<sub>2</sub>O<sub>4</sub>, one obvious weight loss region was observed at 90–110 °C, which was attributed to the desorption of adsorbed water. Meanwhile, the heat absorption peak at 100 °C can be observed on the DSC curve of the pure CoFe<sub>2</sub>O<sub>4</sub> sample. Furthermore, another obvious heat absorption region was observed at 800–900 °C, which may be ascribed to intrinsic magnetic transformation of CoFe<sub>2</sub>O<sub>4</sub>. But this variation of magnetic structure does not lead to obvious weight loss. However, two obvious weight loss steps were observed at 90–110 °C and 215–460 °C for the CoFe<sub>2</sub>O<sub>4</sub>-RGO hybrids, which were ascribed to the loss of adsorbed water and the burnt-out of RGO, respectively. On the basis of the present TG–DSC analysis results, the RGO content in the CoFe<sub>2</sub>O<sub>4</sub>-RGO(35) and CoFe<sub>2</sub>O<sub>4</sub>-RGO(70) samples was ~1.97 and 3.80 wt%, respectively. Moreover, the UV-vis DRS of pure CoFe<sub>2</sub>O<sub>4</sub> and CoFe<sub>2</sub>O<sub>4</sub>-RGO are shown in Fig. S1.† The pure

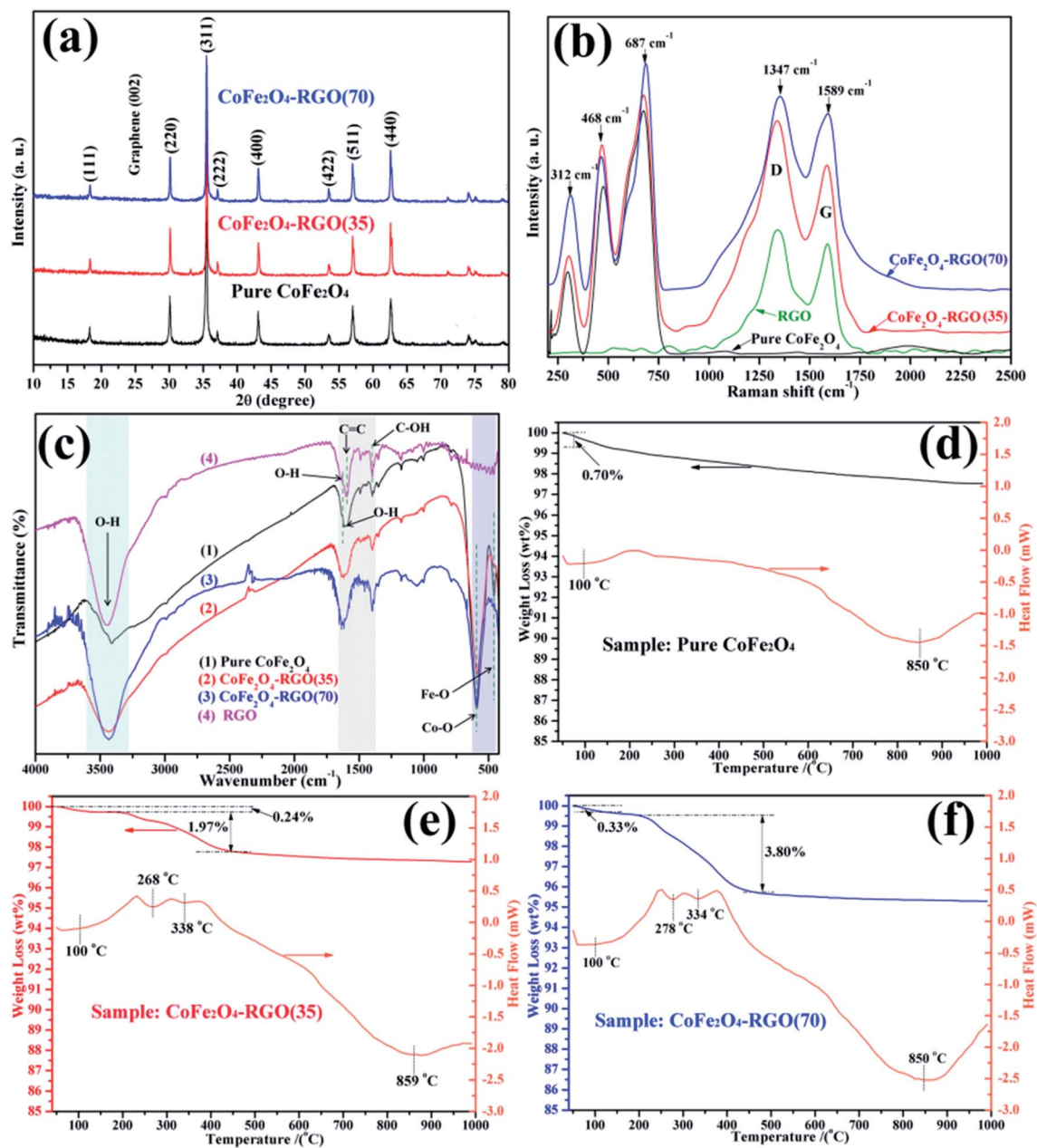


Fig. 1 The crystal structure of the as-synthesized pure  $\text{CoFe}_2\text{O}_4$  and the  $\text{CoFe}_2\text{O}_4$ -RGO hybrids with different amounts of graphene: (a) XRD diffractograms, (b) Raman spectra, (c) FTIR spectra, and (d–f) TG–DSC curves.

$\text{CoFe}_2\text{O}_4$  and  $\text{CoFe}_2\text{O}_4$ -RGO hybrids all exhibit strong absorption in the range of 350–800 nm, which may be due to their black color and narrow bandgap, implying that these materials can act as excellent visible-light-responsive photocatalysts.

To investigate the morphology and composition of the as-fabricated products, the field emission scanning electron microscope (FESEM) and the elemental mapping of the pure  $\text{CoFe}_2\text{O}_4$  and  $\text{CoFe}_2\text{O}_4$ -RGO hybrids were obtained. Two morphological features were observed on the FESEM of the bare  $\text{CoFe}_2\text{O}_4$  NPs, *i.e.* granular and sheet-like, and the individual pure  $\text{CoFe}_2\text{O}_4$  NPs were with a size range of 4–98 nm; however, aggregation of some granular particles occurred, and

this resulted in the formation of a large amount of void space (Fig. 2(a)).

Furthermore, the SEM micrographs of  $\text{CoFe}_2\text{O}_4$ -RGO hybrids contained three distinct morphological features: (i) intimate interfacial connections exist between the individual  $\text{CoFe}_2\text{O}_4$  and the RGO nanosheets, (ii) the  $\text{CoFe}_2\text{O}_4$  particles were mainly composed of regular octahedrons and irregular subunit particles with a broad size distribution. The edge lengths of octahedrons are in the range of 60 to 480 nm, while the sizes of the irregular subunit particles are in the range of 10 to 40 nm, (iii) part of the irregular subunit particles were dispersed on the octahedral  $\text{CoFe}_2\text{O}_4$  and the wrinkled

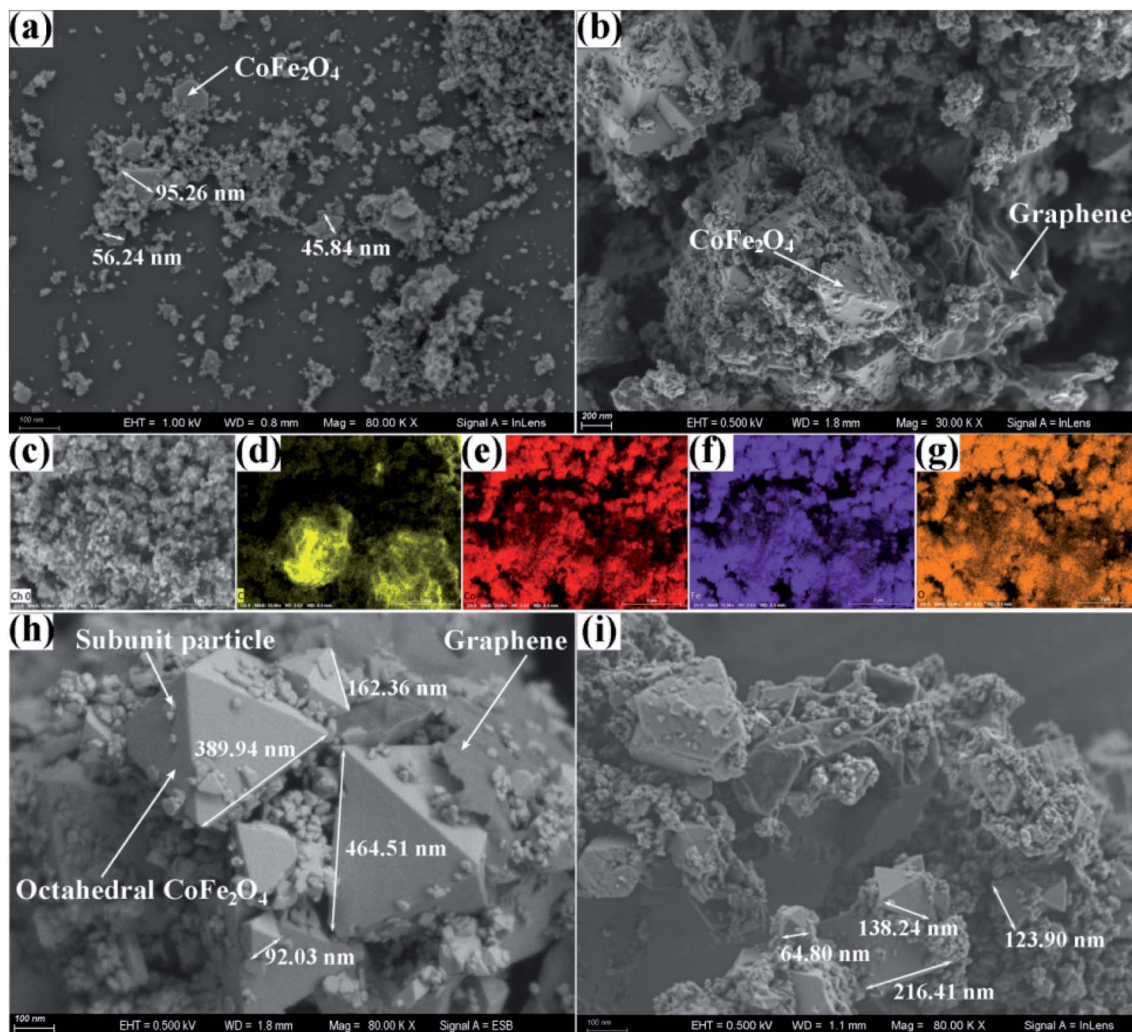


Fig. 2 FESEM micrographs of (a) pure  $\text{CoFe}_2\text{O}_4$ ,  $\text{CoFe}_2\text{O}_4$ -RGO(35) hybrid ((b) low-magnification, (h) high-magnification), and (i)  $\text{CoFe}_2\text{O}_4$ -RGO(70) hybrid. The low-magnification SEM micrograph (c), and the corresponding EDX mapping micrographs of  $\text{CoFe}_2\text{O}_4$ -RGO(35) hybrid for (d) C, (e) Co, (f) Fe, and (g) O.

graphene planes, the other part of subunit particles agglomerated to form nanoclusters (Fig. 2(b, h, and i)).

Compared with the pristine  $\text{CoFe}_2\text{O}_4$ , the average particle size of  $\text{CoFe}_2\text{O}_4$  in the  $\text{CoFe}_2\text{O}_4$ -RGO hybrids was large than that of pure  $\text{CoFe}_2\text{O}_4$  owing to the introduction of graphene sheets. Also, the morphologies of the  $\text{CoFe}_2\text{O}_4$  particles in the  $\text{CoFe}_2\text{O}_4$ -RGO hybrids were different from that of the pristine  $\text{CoFe}_2\text{O}_4$ , *i.e.* it contained octahedrons and irregular subunit particles. This indicates that the hierarchical flexible graphene sheets facilitate the quick growth and Ostwald Ripening of the  $\text{CoFe}_2\text{O}_4$  nanocrystals. In addition, the corresponding EDX mapping micrographs of  $\text{CoFe}_2\text{O}_4$ -RGO(35) hybrid clearly showed that Co, Fe, and O elements were uniformly distributed in the  $\text{CoFe}_2\text{O}_4$  particles, implying the formation of bimetallic oxides but not the formation of simple mixtures of the two corresponding single-metal oxides.<sup>37</sup> Also, it can be seen that the graphene sheets significantly aggregated owing to surface effect that may result in a low specific surface area of the  $\text{CoFe}_2\text{O}_4$ -RGO(35) hybrid.

To further understand the synergistic effects of the  $\text{CoFe}_2\text{O}_4$ -RGO hybrid in photo-Fenton behavior, XPS was used to determine the chemical state of the corresponding transition metal and oxygen in the samples. From the survey spectrum in Fig. 3(a), Fe, Co, O, and C were present in the sample, and no other impurity was detected in the  $\text{CoFe}_2\text{O}_4$ -RGO hybrid. The high-resolution Fe 2p spectra of the pure  $\text{CoFe}_2\text{O}_4$  and  $\text{CoFe}_2\text{O}_4$ -RGO(35) are shown in Fig. 3(b) and (c). For the  $\text{CoFe}_2\text{O}_4$ -RGO(35) sample, the doublets binding energies of Fe 2p<sub>3/2</sub> at 710.3 eV and Fe 2p<sub>1/2</sub> at 723.3 eV are due to the contributions from Fe<sup>3+</sup> ions in the octahedral sites (A-site) of the spinel-type  $\text{CoFe}_2\text{O}_4$ , while the doublets binding energies of Fe 2p<sub>3/2</sub> at 712.7 eV and Fe 2p<sub>1/2</sub> at 724.9 eV are due to the contributions from Fe<sup>3+</sup> ions in the tetrahedral sites (B-site).<sup>38</sup> The Fe 2p spectrum of the  $\text{CoFe}_2\text{O}_4$ -RGO(35) hybrid is nearly identical to that of the high-resolution Fe 2p spectrum of the pristine  $\text{CoFe}_2\text{O}_4$  (Fig. 3(b)), except for a negative shift in the binding energy (Fig. S2†). Also, the high-resolution Co 2p spectrum of  $\text{CoFe}_2\text{O}_4$ -RGO(35) hybrid is nearly identical to that

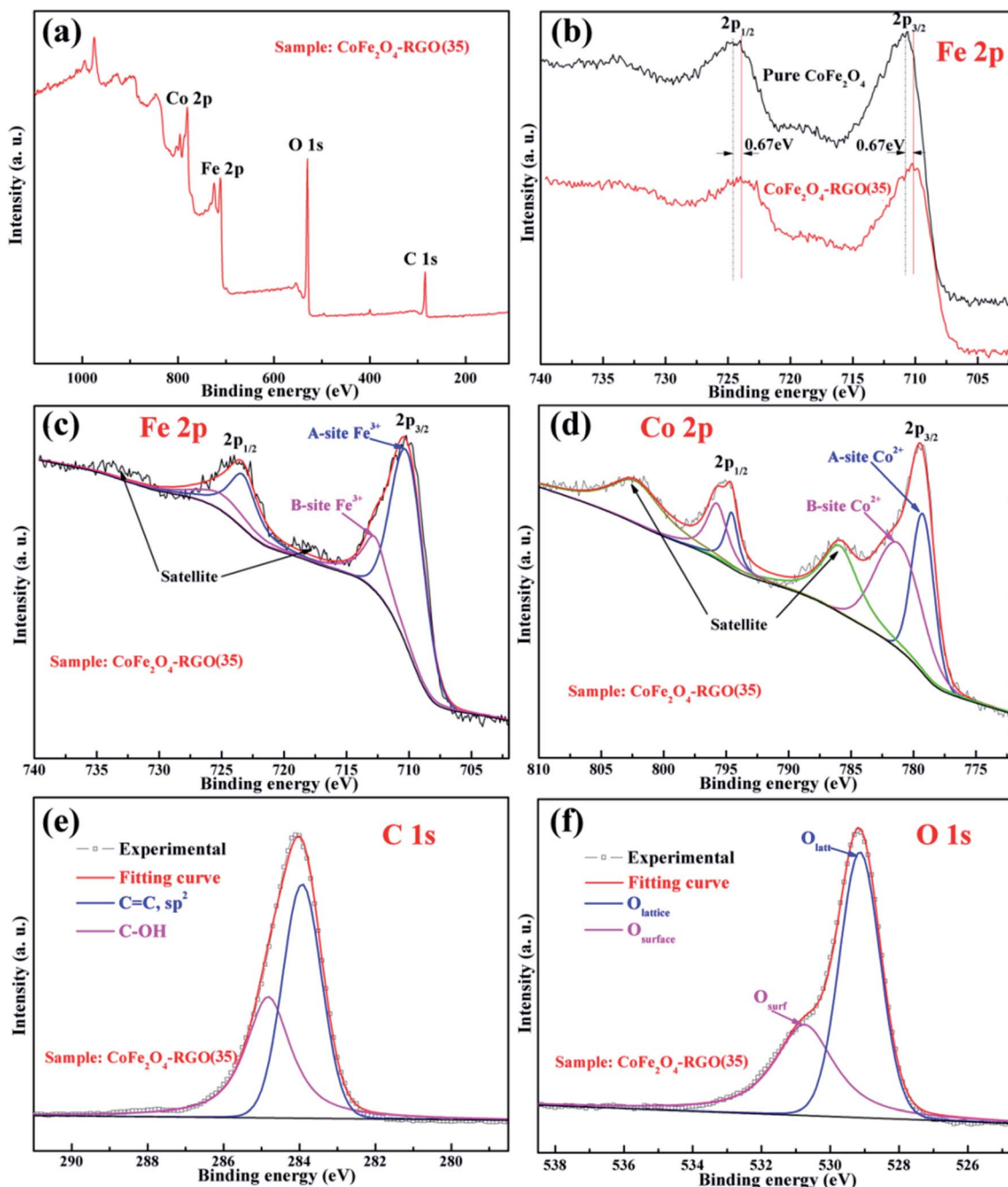


Fig. 3 (a) A survey spectrum of the XPS of  $\text{CoFe}_2\text{O}_4\text{-RGO}(35)$  hybrid, (b) high-resolution Fe 2p XPS analysis of the pure  $\text{CoFe}_2\text{O}_4$  and the  $\text{CoFe}_2\text{O}_4\text{-RGO}(35)$ , and high-resolution XPS spectra of (c) Fe 2p, (d) Co 2p, (e) C 1s, and (f) O 1s of  $\text{CoFe}_2\text{O}_4\text{-RGO}(35)$ .

of the pure  $\text{CoFe}_2\text{O}_4$ , except for a negative shift in the binding energy. These results indicate that efficient charge transfer between the  $\text{CoFe}_2\text{O}_4$  NPs and graphene sheets occurred owing to the intimate interfacial connections, which may be beneficial for the separation of charge carriers.<sup>39</sup>

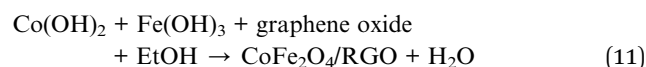
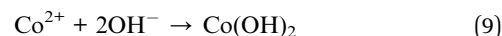
The high-resolution Co 2p spectrum of  $\text{CoFe}_2\text{O}_4\text{-RGO}(35)$  hybrid is similar to its Fe 2p spectrum (Fig. 3(d)); the peaks observed at 779.2 eV ( $\text{Co } 2p_{3/2}$ ) and 794.6 eV ( $\text{Co } 2p_{1/2}$ ) can be assigned to the contributions from  $\text{Co}^{2+}$  ions in the octahedral sites (A-site) while the doublets binding energies of  $\text{Co } 2p_{3/2}$  at

781.2 eV and  $\text{Co } 2p_{1/2}$  at 795.7 eV are ascribed to the contributions from  $\text{Co}^{2+}$  ions in tetrahedral sites (B-site). Compared with the Fe 2p spectrum, there are two obvious shake-up satellite peaks at 785.8 eV and 802.2 eV in the Co 2p spectrum. The presence of these intense satellite signals indicates that a large number of high spin  $\text{Co}^{2+}$  ions occupy the octahedral sites (A-site) in spinel-type  $\text{CoFe}_2\text{O}_4$ .<sup>40,41</sup> Moreover,  $\text{CoFe}_2\text{O}_4$  is a ferromagnetic material with a partially inverse spinel structure.<sup>42</sup> The deconvoluted C 1s spectra of  $\text{CoFe}_2\text{O}_4\text{-RGO}(35)$ , as shown in Fig. 3(e), reveals the presence of oxygen-containing groups (C-

OH, 284.8 eV) and  $sp^2$  carbons (C=C, 283.9 eV).<sup>43</sup> These results are in accordance with the FT-IR and Raman spectroscopy analyzes. The high-resolution O 1s spectra of  $CoFe_2O_4$ -RGO(35) are divided into two individual peaks (Fig. 3(f)); the O 1s peaks at 529.2 and 530.8 eV, which originated from the lattice oxygen atoms (denoted as  $O_{latt}$ ) and surface hydroxyl species or the adsorbed oxygen (denoted as  $O_{surf}$ ).<sup>44,45</sup> In addition, both  $O_{latt}$  and  $O_{surf}$  play an important role in the radical's generation process.<sup>46</sup>

The specific surface area and pore-size distribution of the as-prepared samples were determined using the nitrogen sorption technique. The nitrogen adsorption-desorption isotherms are shown in Fig. 4(a). All the samples exhibit typical II-type curves with steep uptakes ( $P/P_0 > 0.95$ ) and distinct hysteresis loops ( $0.40 < P/P_0 < 0.95$ ), indicating the co-existence of non-ordered mesopores (2–50 nm), and numerous macropores (>50 nm).<sup>47</sup> The primary  $CoFe_2O_4$  NPs are randomly stacked and this results in the creation of macropores. The Brunauer–Emmett–Teller surface areas of  $CoFe_2O_4$ ,  $CoFe_2O_4$ -RGO(35), and  $CoFe_2O_4$ -RGO(70) were 71.20, 35.11, and 40.42  $m^2 g^{-1}$ , respectively. Furthermore, the  $CoFe_2O_4$ -RGO(35) and  $CoFe_2O_4$ -RGO(70) exhibit classical type H3 hysteresis loops, arising from the capillary condensation and slit-shaped type pore structure of the RGO nanosheets.<sup>48</sup> In addition, the specific surface area of graphene oxide (GO) raw material was estimated to be as high as 556.38  $m^2 g^{-1}$  (Fig. S3†). Because the excessive  $CoFe_2O_4$  nanoclusters were anchored on the graphene nanosheets, the specific surface area of  $CoFe_2O_4$ -RGO hybrid was much lower than that of the pure  $CoFe_2O_4$  and GO raw material. The large specific surface area of pure  $CoFe_2O_4$  should enhance its ability to absorb dyes in wastewater. Moreover, the pore-size distribution shown in Fig. 4(b) indicates that the pure  $CoFe_2O_4$  has a broad pore size distribution in the range of 5–20 nm, while the central peak was displayed at approximately 8.6 nm. The  $CoFe_2O_4$ -RGO hybrid exhibited a bimodal pore size distribution owing to the abundant mesoporous channels formed upon the incorporation of layered graphene sheets. For example, a sharp pore size distribution at ~3.6 nm and 6.9 nm were observed for  $CoFe_2O_4$ -RGO(70).

The fabrication process of the octahedral  $CoFe_2O_4$ -RGO hybrids in this study is depicted in Fig. 5. In our study, the growth conditions used to fabricate the octahedral  $CoFe_2O_4$ /RGO hybrids were a high pH (~13) and a relatively long solvothermal time, which is briefly described as follows:



This indicates that the formation of this unique nanohybrid can be controlled in two stages: (i) the formation of  $Co(OH)_2$  and  $Fe(OH)_3$  colloidal particles; it is well known that GO possesses negative charge owing to the existence of numerous oxygen-containing functional groups, such as carboxyl, carbonyl, and hydroxyl.<sup>49</sup> In addition, the oxygen-containing groups on the GO sheets may serve as heterogeneous nucleation sites.<sup>50</sup> When  $Co(NO_3)_2 \cdot 6H_2O$  and  $Fe(NO_3)_3 \cdot 9H_2O$  are added into the GO suspension, the positively charged metal ions ( $Co^{2+}$  and  $Fe^{3+}$ ) would anchor onto the surface of the GO sheets *via* electrostatic attraction. After increasing the pH of the mixed solution by the introduction of sufficient  $OH^-$ , the alkaline conditions promotes the precipitation of  $Co^{2+}$  and  $Fe^{3+}$  ions in ethyl alcohol and this result in the formation of nucleation precursors, *i.e.*  $Co(OH)_2$  and  $Fe(OH)_3$  colloidal particles (eqn (1) and (2)).<sup>51,52</sup> (ii) *in situ* growth of the  $CoFe_2O_4$  crystals and the confining effects of graphene; during the solvothermal treatment, the  $Co(OH)_2$  and  $Fe(OH)_3$ , colloidal particles gradually combine to form  $CoFe_2O_4$  nuclei. Meanwhile, the GO sheets were reduced during the solvothermal reactions (eqn (3)).<sup>53</sup>

To reduce the surface energy, aggregation of many  $CoFe_2O_4$  nanocrystals further occurred.<sup>50,54</sup> It is well known that the  $CoFe_2O_4$  nanocrystals with a broad size distribution may result from the quick nucleation and growth.<sup>38</sup> The  $CoFe_2O_4$  nanocrystals which are tightly anchored onto the graphene sheets

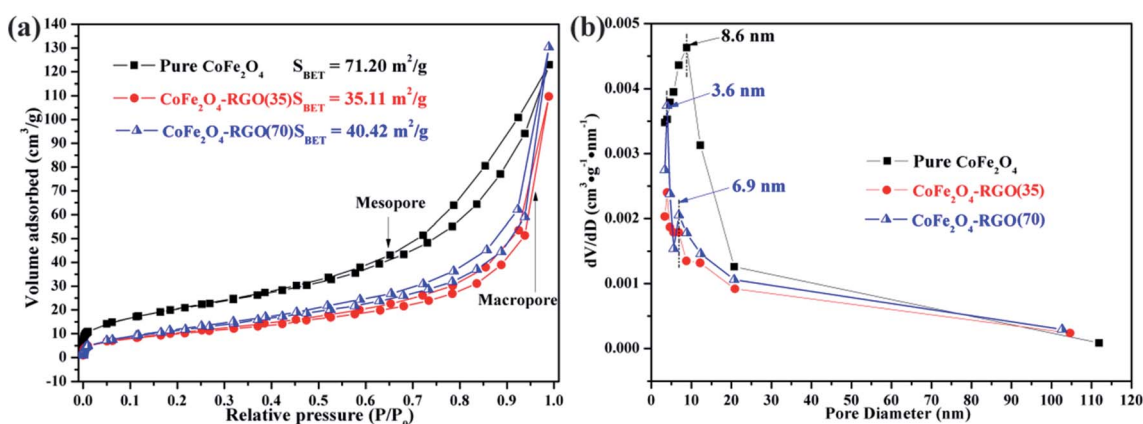


Fig. 4 (a) Nitrogen adsorption-desorption isotherm curves and (b) the corresponding Barrett–Joyner–Halenda pore size distribution of the as-prepared  $CoFe_2O_4$  and  $CoFe_2O_4$ -RGO.

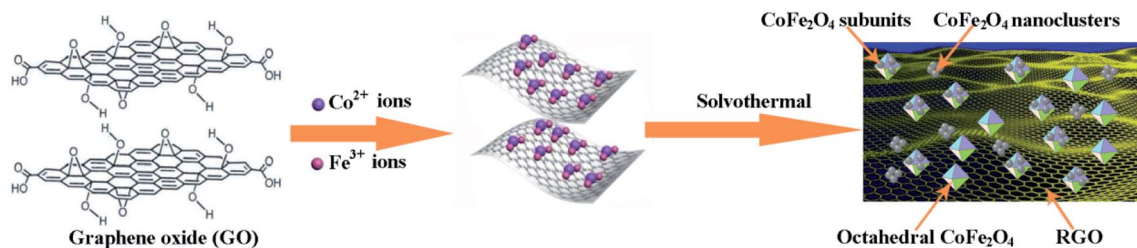


Fig. 5 Schematic of the fabrication process of the octahedral  $\text{CoFe}_2\text{O}_4$ -RGO hybrids.

grew quickly owing to the abundant growth units near the surface of the RGO sheets. Then the octahedral  $\text{CoFe}_2\text{O}_4$  particles, which are formed under high autogenous pressure at  $180^\circ\text{C}$ , are enclosed by the  $\{111\}$  surfaces to achieve the lowest Gibbs free energy. Compared with  $\text{CoFe}_2\text{O}_4$  nanocrystals which tightly anchors itself onto graphene sheets, the growth of the  $\text{CoFe}_2\text{O}_4$  nanocrystals in the mixture solution was slower and it formed irregular  $\text{CoFe}_2\text{O}_4$  nanoclusters. Consequently, the  $\text{CoFe}_2\text{O}_4$  particles within the  $\text{CoFe}_2\text{O}_4$ -RGO hybrids exhibited a more obvious difference in morphology, *i.e.* octahedrons and irregular subunit particles, and the  $\text{CoFe}_2\text{O}_4$ -RGO hybrids were

obtained. However, further experimental evidence is required to verify the present observations.

### 3.2. Catalytic activity

Control experiments were conducted at near-neutral pH conditions (adjusted with phosphate buffer solution) to compare the degradation efficiency of MB dye by the as-prepared sample and  $\text{CoFe}_2\text{O}_4$ -RGO/ $\text{H}_2\text{O}_2$  at various conditions. MB dye was selected as the targeted pollutant owing to its stability under the visible light. Fig. 6(a) and (b) shows the removal efficiency of MB in the presence of either the catalysts

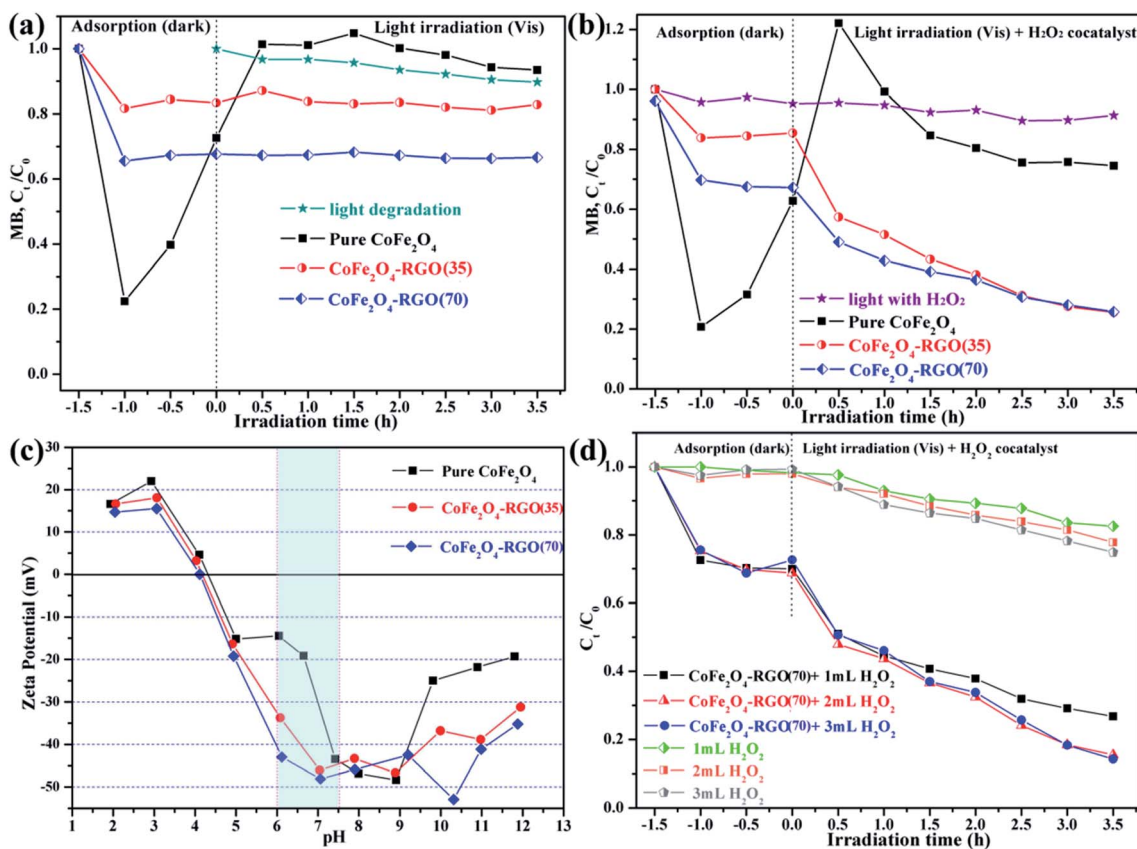


Fig. 6 Photocatalytic degradation of MB by the as-prepared samples alone (a), or the catalysts in conjunction with  $\text{H}_2\text{O}_2$  (b) under visible-light irradiation. Unless otherwise stated, the reaction conditions are:  $[\text{MB}] = 10 \text{ mg L}^{-1}$ , 60 mL MB solution,  $[\text{catalyst}] = 1 \text{ mg mL}^{-1}$ , visible light irradiation ( $\lambda > 420 \text{ nm}$ , 500 W),  $T = 25^\circ\text{C}$ , initial pH = 6.4. (c) Effect of solution pH on the zeta potentials of  $\text{CoFe}_2\text{O}_4$  and  $\text{CoFe}_2\text{O}_4$ -RGO hybrids. (d) MB degradation using  $\text{CoFe}_2\text{O}_4$ -RGO/ $\text{H}_2\text{O}_2$ : effect of hydrogen peroxide dose (reaction conditions:  $[\text{MB}] = 10 \text{ mg L}^{-1}$ , 60 mL MB solution,  $[\text{catalyst}] = 1 \text{ mg mL}^{-1}$ ).



(i.e.  $\text{CoFe}_2\text{O}_4$  and  $\text{CoFe}_2\text{O}_4\text{-RGO}$ ) alone or the catalysts together with 1.0 mL 30 wt%  $\text{H}_2\text{O}_2$  under visible-light irradiation. The adsorption process was conducted by dispersing the products in the MB solution in the dark for 1.5 h and the photodegradation step began at  $t = 0$ . Clearly, the adsorption ability of bare  $\text{CoFe}_2\text{O}_4$  was much higher than that of the  $\text{CoFe}_2\text{O}_4\text{-RGO}$  hybrids owing to the large specific surface area of the  $\text{CoFe}_2\text{O}_4$  sample and the MB molecules having an acceptable molecular size. Interestingly, for bare  $\text{CoFe}_2\text{O}_4$ , the MB molecules were easily re-released into an aqueous solution from its surface after light irradiation or on addition of the  $\text{H}_2\text{O}_2$  co-catalyst, which is consistent with a previous report.<sup>55</sup> The explanation for this observation is that a weak interaction exists between the  $\text{CoFe}_2\text{O}_4$  NPs and MB dye. In addition, the degradation efficiency of the MB solution was rather low in the absence of the photocatalysts.

Fig. 6(a) shows the total removal efficiency of three samples (i.e.  $\text{CoFe}_2\text{O}_4$ ,  $\text{CoFe}_2\text{O}_4\text{-RGO}(35)$ , and  $\text{CoFe}_2\text{O}_4\text{-RGO}(70)$ ) without  $\text{H}_2\text{O}_2$  co-catalyst for MB dye. The order of the removal efficiency is  $\text{CoFe}_2\text{O}_4\text{-RGO}(70) > \text{CoFe}_2\text{O}_4\text{-RGO}(35) > \text{CoFe}_2\text{O}_4$ . The elimination of MB dye by only the catalysts was dominated by the adsorption process due to the  $\pi\text{-}\pi$  stacking between the aromatic dye molecules and the hexagonal regions of

graphene.<sup>56,57</sup> However, with the simultaneous introduction of the as-prepared catalysts and the  $\text{H}_2\text{O}_2$  co-catalyst, the photodegradation of MB was fast and efficient owing to the reaction of photogenerated carriers and  $\text{H}_2\text{O}_2$ .<sup>58</sup> The order of the photodegradation efficiency is  $\text{CoFe}_2\text{O}_4\text{-RGO}(35) > \text{CoFe}_2\text{O}_4\text{-RGO}(70) > \text{CoFe}_2\text{O}_4 > \text{H}_2\text{O}_2$ . During the photodegradation process,  $\text{CoFe}_2\text{O}_4\text{-RGO}(35)$  exhibited the highest MB photodegradation efficiency ( $\sim 43\%$ ) in 3.5 h among all the samples, and the total MB removal efficiency ( $\sim 73\%$ ) was achieved when the  $\text{CoFe}_2\text{O}_4\text{-RGO}(35)/\text{H}_2\text{O}_2$  system was used (Fig. 6(b)).

The adsorption reaction is often related to the surface charge of the NPs. The effect of solution pH on zeta potentials of the  $\text{CoFe}_2\text{O}_4$  and  $\text{CoFe}_2\text{O}_4\text{-RGO}$  hybrids is shown in Fig. 6(c). It can be seen that zeta potentials of the as-prepared particles decreased as the pH increases and that of the  $\text{CoFe}_2\text{O}_4$  and  $\text{CoFe}_2\text{O}_4\text{-RGO}$  hybrids were negatively charged at  $\text{pH} > 4.3$ . In addition, the estimated zeta potentials observed for  $\text{CoFe}_2\text{O}_4$ ,  $\text{CoFe}_2\text{O}_4\text{-RGO}(35)$ , and  $\text{CoFe}_2\text{O}_4\text{-RGO}(70)$  were about  $-19.1$ ,  $-33.7$ , and  $-42.9$  mV at  $\text{pH} = \sim 6.3$ , respectively. Therefore, the adsorption equilibrium rate toward the cationic MB dye of the  $\text{CoFe}_2\text{O}_4\text{-RGO}$  hybrids was more rapid compared to that of the pure  $\text{CoFe}_2\text{O}_4$ . This is because of the strong electrostatic interactions between MB and  $\text{CoFe}_2\text{O}_4\text{-RGO}$  hybrids surfaces. Also,

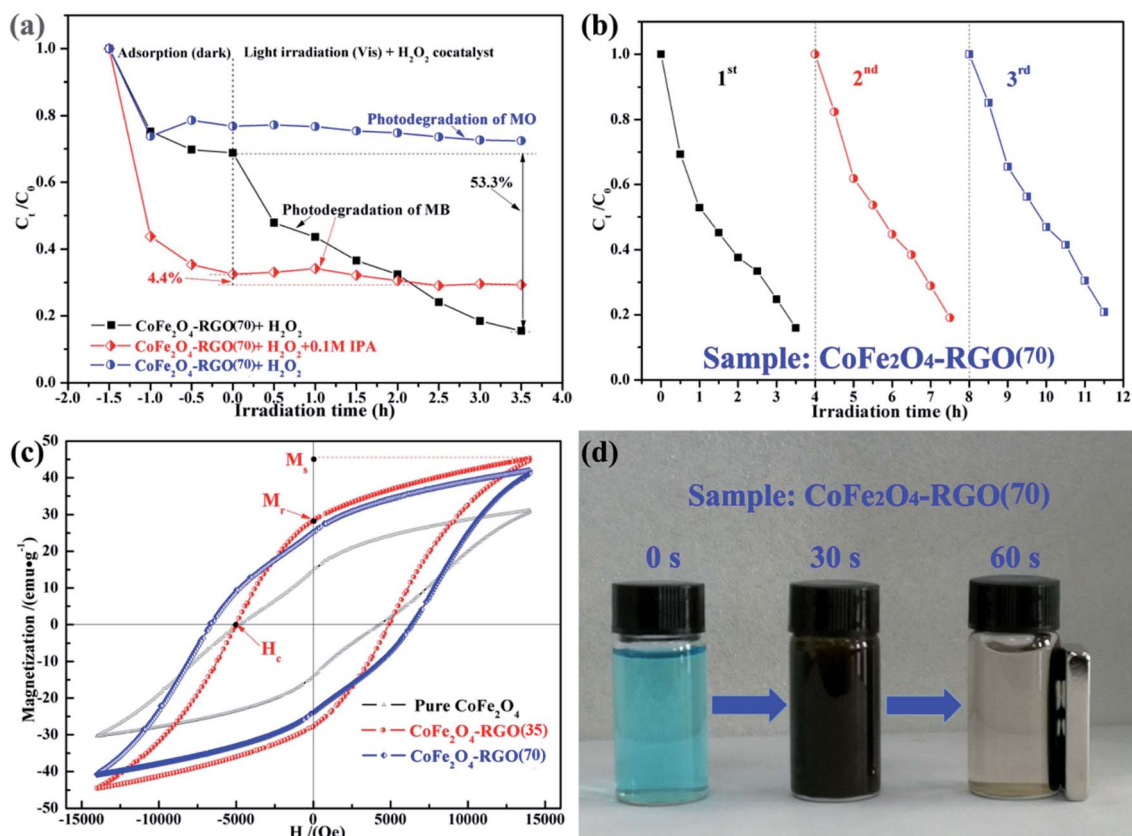
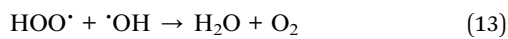
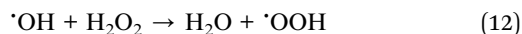


Fig. 7 (a) Effect of IPA and different dyes on the degradation process of " $\text{CoFe}_2\text{O}_4\text{-RGO}(70) + \text{H}_2\text{O}_2$ " system. (b) The performance of the  $\text{CoFe}_2\text{O}_4\text{-RGO}(70)$  hybrids on reuse in the degradation of MB (reaction conditions:  $[\text{MB}] = 10 \text{ mg L}^{-1}$ ,  $[\text{H}_2\text{O}_2] = 0.035 \text{ g mL}^{-1}$ ,  $[\text{catalyst}] = 1 \text{ mg mL}^{-1}$ ,  $T = 25^\circ\text{C}$ ). (c) Magnetization vs. applied magnetic field at room temperature with  $H$  up to 14 kOe for the  $\text{CoFe}_2\text{O}_4$  and  $\text{CoFe}_2\text{O}_4\text{-RGO}$  samples. (d) Digital images of the  $10 \text{ mg L}^{-1}$  MB solution before adsorption and after adsorption at various time (adsorption reaction conditions:  $[\text{MB}] = 10 \text{ mg L}^{-1}$ , 4 mL MB solution,  $[\text{catalyst}] = 0.05 \text{ g mL}^{-1}$ ,  $T = 25^\circ\text{C}$ ).

desorption of the MB molecules from the surface of the CoFe<sub>2</sub>O<sub>4</sub>-RGO hybrids into the aqueous solution was difficult after light irradiation or addition of the H<sub>2</sub>O<sub>2</sub> co-catalyst.

Fig. 6(d) depicts the effect of hydrogen peroxide dose on MB degradation using CoFe<sub>2</sub>O<sub>4</sub>-RGO(70) hybrids. We observed that the concentration of MB reduced slowly under light irradiation for the “visible light with H<sub>2</sub>O<sub>2</sub>” system. The introduction of H<sub>2</sub>O<sub>2</sub> weakly improves the photocatalytic effects by increasing the addition level of H<sub>2</sub>O<sub>2</sub> in current experiment, *e.g.* from 1 mL to 2 mL and from 2 mL to 3 mL under visible light irradiations for 3.5 h, the degradation rate of MB can be slightly increased to 22.2% and 25.14%, respectively. This result indicates that the degradation rate of MB could not be significantly improved by simply increasing the content of H<sub>2</sub>O<sub>2</sub>. Compared with the “visible light with H<sub>2</sub>O<sub>2</sub>” system, a faster and more efficient degradation of MB solution occurred in the “CoFe<sub>2</sub>O<sub>4</sub>-RGO(70) + H<sub>2</sub>O<sub>2</sub>” system. Obviously, the introduction of 2 mL H<sub>2</sub>O<sub>2</sub> remarkably promotes the photo-Fenton catalytic activity, the removal rate of MB can be further increased to 84.5%. In addition, the optimum amount of H<sub>2</sub>O<sub>2</sub> is always present in the Fenton-like reaction system. Previous work have shown that the addition of excessive H<sub>2</sub>O<sub>2</sub> may result in scavenging of the hydroxyl radicals (<sup>•</sup>OH), thus not only reducing the photo-Fenton reaction rate but also causing the wastage of H<sub>2</sub>O<sub>2</sub> (eqn (12) and (13)).<sup>59</sup>



The heterogeneous photo-Fenton mechanism of the “CoFe<sub>2</sub>O<sub>4</sub>-RGO + H<sub>2</sub>O<sub>2</sub>” system will be discussed in a later section of this paper.

To identify the main active species for the degradation of dyes in the “CoFe<sub>2</sub>O<sub>4</sub>-RGO(70) + H<sub>2</sub>O<sub>2</sub>” system, IPA was separately added into the system as a scavenger of hydroxyl radicals (<sup>•</sup>OH).<sup>60</sup> As shown in Fig. 7(a), the dye removal efficiency of the CoFe<sub>2</sub>O<sub>4</sub>-RGO(70) for MB was higher than that of MO. In addition, the adsorption and photodegradation rate of the CoFe<sub>2</sub>O<sub>4</sub>-RGO(70) hybrid for the anionic dye (MO) was lower when compared with that of the cationic dye (MB), and this was attributed to the repulsive forces that exist between MO and the -OH/R-COO<sup>-</sup> groups on the surface of CoFe<sub>2</sub>O<sub>4</sub>-RGO(70) hybrid.<sup>48</sup> Furthermore, the original photodegradation rate is high, *i.e.* without adding a quenching agent into the reaction solution, and the degree of MB photodegradation was as high as 53.3%. However, the degradation of MB was obviously inhibited by the introduction of 0.1 M IPA, which resulted in a decrease in the degree of MB photodegradation to 4.4% within 3.5 h. This result clearly proved that <sup>•</sup>OH is the dominating reactive species in the “CoFe<sub>2</sub>O<sub>4</sub>-RGO + H<sub>2</sub>O<sub>2</sub>” system, and it contributes to the decolorization of MB.

The recyclability and stability of the catalyst are important parameters for its commercialization. To evaluate the reusability of our catalytic system, three rounds of the photodegradation reaction for MB dye were conducted with the recyclable CoFe<sub>2</sub>O<sub>4</sub>-RGO(70) hybrid under the same reaction

conditions. After each cycle, the catalyst was separated from the reaction solution using an external magnet, and it was washed several times with deionized water and ethanol. As shown in Fig. 7(b), the removal efficiencies for MB in the third cycle was nearly the same as that of the first two cycles. Although the activity of the CoFe<sub>2</sub>O<sub>4</sub>-RGO(70) hybrid slightly decreased in the third cycle, the removal efficiencies for MB was still 79.2%. The slight loss of the photodegradation activity may be due to the loss of the catalysts during the recovery process or the weak decoration of CoFe<sub>2</sub>O<sub>4</sub> and RGO.<sup>37,53</sup> All these analyses indicate that CoFe<sub>2</sub>O<sub>4</sub>-RGO hybrid is still highly efficient, arising from the graphene/CoFe<sub>2</sub>O<sub>4</sub> heterojunction and the lowest energy {111} facets of octahedral CoFe<sub>2</sub>O<sub>4</sub>, when reused.

The magnetic hysteresis loops of the pure CoFe<sub>2</sub>O<sub>4</sub> and the CoFe<sub>2</sub>O<sub>4</sub>-RGO hybrids were conducted using a vibrating sample magnetometer (VSM) from -14 000 to 14 000 Oe at room temperature, as shown in Fig. 7(c). All the samples exhibit ferromagnetic behavior. The saturation magnetization (*M<sub>s</sub>*) value of the pure CoFe<sub>2</sub>O<sub>4</sub> nanocrystals is approximately 31.15 emu g<sup>-1</sup>, which is lower than that of the CoFe<sub>2</sub>O<sub>4</sub>-RGO hybrids (41.98–45.14 emu g<sup>-1</sup>). Compared with the bare CoFe<sub>2</sub>O<sub>4</sub> NPs, the enhancement of the *M<sub>s</sub>* for CoFe<sub>2</sub>O<sub>4</sub>-RGO hybrids was mainly due to the larger average particle size of the octahedral CoFe<sub>2</sub>O<sub>4</sub> nanocrystals.<sup>61,62</sup> Hence, more efficient separation of CoFe<sub>2</sub>O<sub>4</sub>-RGO hybrids is possible.<sup>23</sup> As shown in Fig. 7(d), the first bottle (marked with 0 s) is the initial MB (10 mg L<sup>-1</sup>) solution without CoFe<sub>2</sub>O<sub>4</sub>-RGO(70) catalyst. The CoFe<sub>2</sub>O<sub>4</sub>-RGO hybrids were uniformly dispersed in MB solution to form a dark brown suspension (marked with 30 s). However, when an external magnet was placed close to the bottle, the synthesized samples which had absorbed MB from the aqueous solution were rapidly separated from the aqueous media (marked with 60 s). Thus, the CoFe<sub>2</sub>O<sub>4</sub>-RGO catalyst is quite acceptable owing to its good separation ability. In addition, the *M<sub>s</sub>* values of the samples were lower than that of the bulk counterpart (74 emu g<sup>-1</sup>), which may be ascribed to the possible effect of surface spin canting on the CoFe<sub>2</sub>O<sub>4</sub> NPs as well as the weight-fraction of the RGO.<sup>63</sup> Moreover, the field-dependent magnetization curves of the CoFe<sub>2</sub>O<sub>4</sub> and CoFe<sub>2</sub>O<sub>4</sub>-RGO hybrids exhibit non-negligible remanence (*M<sub>r</sub>* = 14.92–25.42 emu g<sup>-1</sup>) and high coercivity (*H<sub>c</sub>* = 4.32–6.41 kOe), indicating that they are hard magnetic materials (Table S1†).

### 3.3. Activation mechanism

Based on the information above, we propose an activation mechanism of H<sub>2</sub>O<sub>2</sub> by the CoFe<sub>2</sub>O<sub>4</sub>-RGO hybrids, as presented in Fig. 8. Clearly, the main active sites of CoFe<sub>2</sub>O<sub>4</sub>-RGO hybrids are the cobalt and iron ions (Co<sup>2+/3+</sup> and Fe<sup>3+/2+</sup>) in a spinel-type CoFe<sub>2</sub>O<sub>4</sub> surface lattice. When the CoFe<sub>2</sub>O<sub>4</sub> particles are excited using a daylight lamp, electron-hole pairs are produced on the surface of the CoFe<sub>2</sub>O<sub>4</sub> particles (eqn (14)). The presence of highly conductive RGO in the CoFe<sub>2</sub>O<sub>4</sub>-RGO hybrids can inhibit the recombination of electrons and holes because electrons are quickly transferred to the RGO sheets due to a percolation mechanism (eqn (15)).<sup>20</sup> Then the photogenerated electrons within the graphene sheets could be captured by H<sub>2</sub>O<sub>2</sub> to

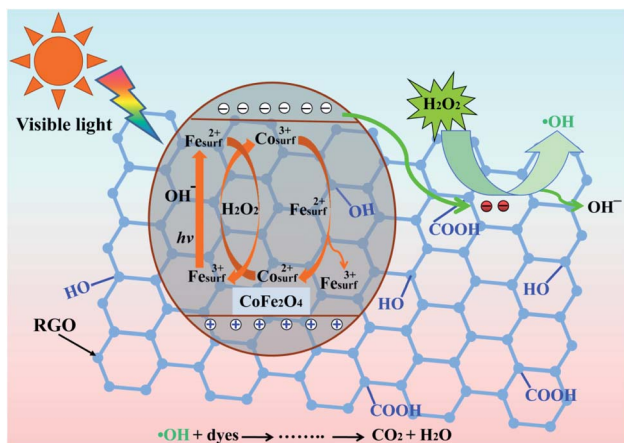
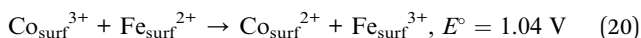
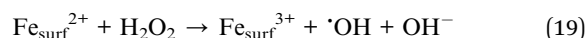
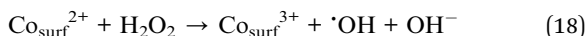
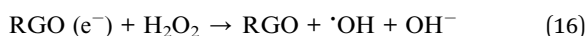
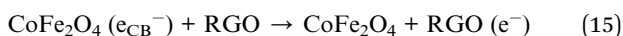
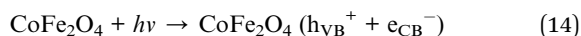


Fig. 8 Schematic illustration of an active heterogeneous photo-Fenton mechanism based on  $\text{CoFe}_2\text{O}_4$ -RGO hybrids.

generate  $\cdot\text{OH}$  (eqn (16)).<sup>64</sup> Meanwhile, the photogenerated holes can participate in the photo-Fenton reaction to yield  $\cdot\text{OH}$  (eqn (17)).<sup>65</sup> Furthermore, the reaction of  $\text{H}_2\text{O}_2$  with cobalt and iron ions generate a Fenton reagent which yields hydroxyl radical ( $\cdot\text{OH}$ ) (eqn (18) and (19)).<sup>19,66</sup> The thermodynamic reduction of  $\text{Co}^{3+}$  by  $\text{Fe}^{2+}$  is represented by eqn (20). Efficient regeneration of the surface  $\text{Co}^{2+}$  may be responsible for the significant increase in the activity of  $\text{H}_2\text{O}_2$ .<sup>19</sup>



Since  $\cdot\text{OH}$  is produced through four pathways, an enhancement in the photodegradation rate was observed. Therefore, the hydroxyl radical ( $\cdot\text{OH}$ ), which generated in the photo-Fenton reaction, is the main active species for the degradation of the dyes.

## 4. Conclusions

In this study, we have described a feasible one-pot solvothermal method to fabricate novel octahedral  $\text{CoFe}_2\text{O}_4$ -RGO hybrids. These catalysts exhibited excellent  $\text{H}_2\text{O}_2$  activity for the degradation of MB dye at nearly neutral pH and room temperature. On screening the catalyst, we observed that  $\text{CoFe}_2\text{O}_4$ -RGO(35) and  $\text{CoFe}_2\text{O}_4$ -RGO(70) hybrids exhibited superior photo-Fenton activity for the removal of MB when compared with pure

$\text{CoFe}_2\text{O}_4$ . We demonstrated that  $\cdot\text{OH}$  is the dominating reactive species in the “ $\text{CoFe}_2\text{O}_4$ -RGO +  $\text{H}_2\text{O}_2$ ” heterogeneous photo-Fenton system, and it is responsible for the decolorization of MB. In addition, the high catalytic activity of  $\text{CoFe}_2\text{O}_4$ -RGO(70) hybrids was attributed to the synergistic effect of redox  $\text{Co}^{2+/3+}$  and  $\text{Fe}^{3+/2+}$  pairs. Based on the results obtained from the experiment conducted, we proposed an activation mechanism of  $\text{H}_2\text{O}_2$  by the  $\text{CoFe}_2\text{O}_4$ -RGO hybrids. In view of the excellent catalytic activity, the outstanding reusability and stability, as well as the magnetic recyclability of  $\text{CoFe}_2\text{O}_4$ -RGO hybrid, it can potentially be applied in advanced oxidation processes as a heterogeneous photo-Fenton catalyst.

## Conflicts of interest

There are no conflicts to declare.

## Acknowledgements

This study was supported by the Science and Technology Research Project of Jiangxi Education Department in 2019 (GJJ190585), the Natural Science Foundation of Jiangxi Province (20202BABL204016), Science and Technology Research Project of Jiangxi Education Department (GJJ180608), School Youth Top Talent Program of JXSTNU (2018QNBjRC005).

## References

- B. D. C. Ventura-camargo and M. A. Marin-morales, Azo Dyes: Characterization and toxicity-A review, *Text. Light Ind. Sci. Tech.*, 2013, **2**, 85–103.
- F. Brandl, N. Bertrand, E. Martins and R. Langer, Nanoparticles with photoinduced precipitation for the extraction of pollutants from water and soil, *Nat. Commun.*, 2015, **6**, 7765.
- Y. W. Zhu, S. T. Murali, W. W. Cai, X. S. Li, *et al.*, Graphene and graphene oxide: Synthesis, properties, and applications, *Adv. Mater.*, 2010, **22**, 3906–3924.
- I. Duru, D. Ege and A. R. Kamali, Graphene oxides for removal of heavy and precious metals from wastewater, *J. Mater. Sci.*, 2016, **51**, 6097–6116.
- B. Liang, P. Zhang, J. Q. Wang, J. Qu, L. F. Wang, X. X. Wang, C. F. Guan and K. Pan, Membranes with selective laminar nanochannels of modified reduced graphene oxide for water purification, *Carbon*, 2016, **103**, 94–100.
- W. Z. Yin, S. Hao and H. Q. Cao, Solvothermal synthesis of magnetic  $\text{CoFe}_2\text{O}_4$ /rGO nanocomposites for highly efficient dye removal in wastewater, *RSC Adv.*, 2017, **7**, 4062–4069.
- S. S. Gao, L. Liu, Y. K. Tang, D. Z. Jia, Z. B. Zhao and Y. Y. Wang, Coal based magnetic activated carbon as a high performance adsorbent for methylene blue, *J. Porous Mater.*, 2016, **23**, 877–884.
- A. A. Markeb, L. A. Ordosgoitia, A. Alonso, A. Sanchez and X. Font, Novel magnetic core-shell Ce-Ti@ $\text{Fe}_3\text{O}_4$  nanoparticles as an adsorbent for water contaminants removal, *RSC Adv.*, 2016, **6**, 6913–6917.

- 9 L. Gan, S. M. Shang, C. W. M. Yuen, *et al.*, Hydrothermal synthesis of magnetic CoFe<sub>2</sub>O<sub>4</sub>/graphene nanocomposites with improved photocatalytic activity, *Appl. Surf. Sci.*, 2015, **351**, 140–147.
- 10 Y. Zhang, B. Chen, L. Zhang, J. Huang, F. H. Chen, *et al.*, Controlled assembly of Fe<sub>3</sub>O<sub>4</sub> magnetic nano-particles on graphene oxide, *Nanoscale*, 2011, **3**, 1446–1450.
- 11 Y. J. Yao, S. D. Miao, S. Z. Liu, L. P. Ma, *et al.*, Synthesis, characterization, and adsorption properties of magnetic Fe<sub>3</sub>O<sub>4</sub>@graphene nanocomposite, *Chem. Eng. J.*, 2012, **184**, 326–332.
- 12 Y. S. Fu and X. Wang, Magnetically separable ZnFe<sub>2</sub>O<sub>4</sub>-graphene catalyst and its high photocatalytic performance under visible light irradiation, *Ind. Eng. Chem. Res.*, 2011, **50**, 7210–7218.
- 13 Y. S. Fu, H. Q. Chen, X. Q. Sun and X. Wang, Graphene-supported nickel ferrite: A magnetically separable photocatalyst with high activity under visible light, *AIChE J.*, 2012, **58**, 3298–3305.
- 14 Y. S. Fu, H. Q. Chen, X. Q. Sun and X. Wang, Combination of cobalt ferrite and graphene: high-performance and recyclable visible-light photocatalysis, *Appl. Catal., B*, 2012, **280**, 111–112.
- 15 Y. S. Fu, P. Xiong, H. Q. Chen, X. Q. Sun and X. Wang, High Photocatalytic activity of magnetically separable manganese ferrite-graphene heteroarchitectures, *Ind. Eng. Chem. Res.*, 2012, **51**, 725–731.
- 16 L. G. Devi and M. Srinivas, Impact of preparative pH conditions on the structure and morphology of graphene oxide-CoFe<sub>2</sub>O<sub>4</sub> composite: Exploration of adsorption isotherm models and photocatalysis, *Surf. Interfaces*, 2019, **14**, 175–183.
- 17 N. W. Li, M. B. Zheng, X. F. Chang, G. B. Ji, H. L. Lu, L. P. Xue, L. J. Pan and J. M. Cao, Preparation of magnetic CoFe<sub>2</sub>O<sub>4</sub>-functionalized graphene sheets *via* a facile hydrothermal method and their adsorption properties, *J. Solid State Chem.*, 2011, **184**, 953–958.
- 18 H. Zheng, J. Wang, S. E. Lofland, Z. Mohaddes-Ardabili, L. Ma, T. Zhao, L. Salamanca-Riba, S. R. Shinde, S. B. Ogale, F. Bai, D. Viehland, Y. Jia, D. G. Schlom, M. Wuttig, A. Roytburd and R. Ramesh, Multiferritic BaTiO<sub>3</sub>-CoFe<sub>2</sub>O<sub>4</sub> nanostructures, *Science*, 2004, **303**, 661–663.
- 19 R. C. C. Costa, M. F. F. Leles, L. C. A. Oliveira, *et al.*, Novel active heterogeneous Fenton system based on Fe<sub>3-x</sub>M<sub>x</sub>O<sub>4</sub> (Fe, Co, Mn, Ni): The role of M<sup>2+</sup> species on the reactivity towards H<sub>2</sub>O<sub>2</sub> reactions, *J. Hazard. Mater. B*, 2006, **129**, 171–178.
- 20 D. Moitra, M. Chandel, B. K. Ghosh, *et al.*, A simple 'in situ' co-precipitation method for the preparation of multifunctional CoFe<sub>2</sub>O<sub>4</sub>-reduced graphene oxide nanocomposites: excellent microwave absorber and highly efficient magnetically separable recyclable photocatalyst for dye degradation, *RSC Adv.*, 2016, **6**, 76759–76772.
- 21 R. Tabit, O. Amadine, Y. Essamlali, *et al.*, Magnetic CoFe<sub>2</sub>O<sub>4</sub> nanoparticles supported on graphene oxide (CoFe<sub>2</sub>O<sub>4</sub>/GO) with high catalytic activity for peroxymonosulfate activation and degradation of rhodamine B, *RSC Adv.*, 2018, **8**, 1351–1360.
- 22 Q. Yang, H. Choi, S. R. Al-Abed and D. D. Dionysiou, Iron-cobalt mixed oxide nanocatalysts: Heterogeneous peroxymonosulfate activation, cobalt leaching, and ferromagnetic properties for environmental applications, *Appl. Catal., B*, 2009, **88**, 462–469.
- 23 L. Gomathi Devi and M. Srinivas, Hydrothermal synthesis of reduced graphene oxide-CoFe<sub>2</sub>O<sub>4</sub> heteroarchitecture for high visible light photocatalytic activity: Exploration of efficiency, stability and mechanistic pathways, *J. Environ. Chem. Eng.*, 2017, **5**, 3243–3255.
- 24 G. P. Anipsitakis, D. D. Dionysiou and M. A. Gonzalez, Cobalt-mediated activation of peroxymonosulfate and sulfate radical attack on phenolic compounds. Implications of chloride ions, *Environ. Sci. Technol.*, 2006, **40**, 1000–1007.
- 25 Y. J. Yao, J. C. Qin, Y. M. Cai, F. Y. Wei, *et al.*, Facile synthesis of magnetic ZnFe<sub>2</sub>O<sub>4</sub>-reduced graphene oxide hybrid and its photo-Fenton-like behavior under visible irradiation, *Environ. Sci. Pollut. Res.*, 2014, **21**, 7296–7306.
- 26 H. Yi, D. Jiang, J. Chen and Y. Zhang, Evaluation of MnO<sub>2</sub>-templated iron oxide-coated diatomites for their catalytic performance in heterogeneous photo-Fenton-like system, *J. Hazard. Mater.*, 2018, **344**, 230–240.
- 27 H.-Y. He and J. Lu, Highly photocatalytic activities of magnetically separable reduced graphene oxide-CoFe<sub>2</sub>O<sub>4</sub> hybrid nanostructures in dye photodegradation, *Sep. Purif. Technol.*, 2017, **172**, 374–381.
- 28 L. H. Ai, H. Y. Huang, Z. L. Chen, X. Wei, *et al.*, Activated carbon/CoFe<sub>2</sub>O<sub>4</sub> composites: Facile synthesis, magnetic performance and their potential application for the removal of malachite green from water, *Chem. Eng. J.*, 2010, **156**, 243–249.
- 29 Y. J. Yao, Z. H. Yang, D. W. Zhang, W. C. Peng, H. Q. Sun and S. B. Wang, Magnetic CoFe<sub>2</sub>O<sub>4</sub>-graphene hybrids: Facile synthesis, characterization and catalytic properties, *Ind. Eng. Chem. Res.*, 2012, **51**, 6044–6051.
- 30 Z. Ding, W. Wang, Y. J. Zhang, F. Li and J. P. Liu, Synthesis, characterization and adsorption capability for Congo red of CoFe<sub>2</sub>O<sub>4</sub> ferrite nanoparticles, *J. Alloys Compd.*, 2015, **640**, 362–370.
- 31 T. N. Lambert, C. A. Chavez, B. Hernandez-Sanchez, *et al.*, Synthesis and characterization of titania-graphene nanocomposites, *J. Phys. Chem. C*, 2009, **113**, 19812–19823.
- 32 D. Wu, W. Wang, F. Tan, F. Sun, *et al.*, Fabrication of pit-structured ZnO nanorods and their enhanced photocatalytic performance, *RSC Adv.*, 2013, **3**, 20054–20059.
- 33 G. Y. He, J. J. Ding, J. G. Zhang, Q. L. Hao and H. Q. Chen, One-step ball-milling preparation of highly photocatalytic active CoFe<sub>2</sub>O<sub>4</sub>-reduced graphene oxide heterojunctions for organic dye removal, *Ind. Eng. Chem. Res.*, 2015, **54**, 2862–2867.
- 34 G. Srinivas, J. W. Burrell, J. Ford and T. Yildirim, Porous graphene oxide frameworks: synthesis and gas sorption properties, *J. Mater. Chem.*, 2011, **21**, 11323–11329.

- 35 Y. Hou, X. Li, Q. Zhao and G. Chen, ZnFe<sub>2</sub>O<sub>4</sub> multi-porous microbricks/graphene hybrid photocatalyst, Facile synthesis, improved activity and photocatalytic mechanism, *Appl. Catal., B*, 2013, **142**, 80–88.
- 36 A. Meidanchi and O. Akhavan, Superparamagnetic zinc ferrite spinel-graphene nanostructures for fast wastewater purification, *Carbon*, 2014, **69**, 230–238.
- 37 Y. J. Yao, Y. M. Cai, G. D. Wu, F. Y. Wei, X. Y. Li, H. Chen and S. B. Wang, Sulfate radicals induced from peroxymonosulfate by cobalt manganese oxides (Co<sub>x</sub>Mn<sub>3-x</sub>O<sub>4</sub>) for Fenton-like reaction in water, *J. Hazard. Mater.*, 2015, **296**, 128–137.
- 38 H. M. Sun, X. J. Yang, L. J. Zhao, T. H. Xu and J. S. Lian, One-pot hydrothermal synthesis of octahedral CoFe/CoFe<sub>2</sub>O<sub>4</sub> submicron composites as heterogeneous catalysts with enhanced peroxymonosulfate activity, *J. Mater. Chem. A*, 2016, **4**, 9455–9465.
- 39 Z. M. Pan, G. G. Zhang and X. C. Wang, Polymeric carbon nitride/RGO/Fe<sub>2</sub>O<sub>3</sub>: All solid state Z-scheme system for photocatalytic overall water splitting, *Angew. Chem., Int. Ed.*, 2019, **58**, 7102–7106.
- 40 J. G. Kim, D. L. Pugmire, D. Battaglia and M. A. Langell, Analysis of the NiCo<sub>2</sub>O<sub>4</sub> spinel surface with Auger and X-ray photoelectron spectroscopy, *Appl. Surf. Sci.*, 2000, **165**, 70–84.
- 41 Z. P. Zhou, Y. Zhang, Z. Y. Wang, W. Wei, W. F. Tang, J. Shi and R. Xiong, Electronic structure studies of the spinel CoFe<sub>2</sub>O<sub>4</sub> by X-ray photoelectron spectroscopy, *Appl. Surf. Sci.*, 2008, **254**, 6972–6975.
- 42 K. V. Shafi, A. Gedanken, R. Prozorov and J. Balogh, Sonochemical preparation and size-dependent properties of nanostructured CoFe<sub>2</sub>O<sub>4</sub> particles, *Chem. Mater.*, 1998, **10**, 3445–3450.
- 43 D. Zhao, G. Sheng, C. Chen, *et al.*, Enhanced photocatalytic degradation of methylene blue under visible irradiation on graphene@TiO<sub>2</sub> dyade structure, *Appl. Catal., B*, 2012, **111**, 303–308.
- 44 Z. Huang, H. Bao, Y. Yao, W. Lu and W. Chen, Novel green activation processes and mechanism of peroxymonosulfate based on supported cobalt phthalocyanine catalyst, *Appl. Catal., B*, 2014, **154**, 36–43.
- 45 D. Xu, F. Cheng, Q. Lu and P. Dai, Microwave enhanced catalytic degradation of methyl orange in aqueous solution over CuO/CeO<sub>2</sub> catalyst in the absence and presence of H<sub>2</sub>O<sub>2</sub>, *Ind. Eng. Chem. Res.*, 2014, **53**, 2625–2632.
- 46 Y. Ren, L. Lin, J. Ma, J. Yang, J. Feng and Z. Fan, Sulfate radicals induced from peroxymonosulfate by magnetic ferrosinell MFe<sub>2</sub>O<sub>4</sub> (M=Co, Cu, Mn, and Zn) as heterogeneous catalysts in the water, *Appl. Catal., B*, 2015, **165**, 572–578.
- 47 J. Zhao, H. Lai, Z. Lv, *et al.*, Hydrophilic hierarchical nitrogen-doped carbon nanocages for ultrahigh supercapacitive performance, *Adv. Mater.*, 2015, **27**, 3541–3545.
- 48 J. P. Ai, L. L. Hu, Z. H. Zhou, *et al.*, Surfactant-free synthesis of a novel octahedral ZnFe<sub>2</sub>O<sub>4</sub>/grapheme composite with high adsorption and good photocatalytic activity for efficient treatment of dye wastewater, *Ceram. Int.*, 2020, **46**, 11786–11798.
- 49 D. Lu, Y. Zhang, S. Lin, L. Wang and C. Wang, Synthesis of magnetic ZnFe<sub>2</sub>O<sub>4</sub>/graphene composites and its application in photocatalytic degradation of dyes, *J. Alloys Compd.*, 2013, **579**, 336–342.
- 50 S. Y. Liu, J. Xie, C. C. Fang, *et al.*, Self-assembly of a CoFe<sub>2</sub>O<sub>4</sub>/graphene sandwich by a controllable and general route: towards a high-performance anode for Li-ion batteries, *J. Mater. Chem.*, 2012, **22**, 19738–19743.
- 51 W. Q. Jiang, Z. Cao, R. Gu, X. Z. Ye, C. F. Jiang and X. D. Gong, A simple route to synthesize ZnFe<sub>2</sub>O<sub>4</sub> hollow spheres and their magnetorheological characteristics, *Smart Mater. Struct.*, 2009, **18**, 125013.
- 52 T. Zhu, B. Y. Xia, L. Zhou and X. W. Lou, Arrays of ultrafine CuS nanoneedles supported on a CNT backbone for application in supercapacitors, *J. Mater. Chem.*, 2012, **22**, 7851–7855.
- 53 W. Yin, S. Hao and H. Cao, Solvothermal synthesis of magnetic CoFe<sub>2</sub>O<sub>4</sub>/rGO nanocomposites for highly efficient dye removal in wastewater, *RSC Adv.*, 2017, **7**, 4062–4069.
- 54 B. B. Wang, G. Wang, Z. Y. Lv and H. Wang, In situ synthesis of hierarchical CoFe<sub>2</sub>O<sub>4</sub> nanoclusters/grapheme aerogels and their high performance for lithium-ion batteries, *Phys. Chem. Chem. Phys.*, 2015, **17**, 27109–27117.
- 55 Y. Q. Shi, K. Q. Zhou, B. B. Wang, *et al.*, Ternary graphene-CoFe<sub>2</sub>O<sub>4</sub>/CdS nanohybrids: preparation and application as recyclable photocatalysts, *J. Mater. Chem. A*, 2014, **2**, 535–544.
- 56 S. Bai, X. P. Shen, X. Zhong, Y. Liu, *et al.*, One-pot solvothermal preparation of magnetic reduced graphene oxide-ferrite hybrids for organic dye removal, *Carbon*, 2012, **50**, 2337–2346.
- 57 Y. M. Shao, L. C. Zhou, C. Bao and J. J. Ma, A facile approach to the fabrication of rattle-type magnetic carbon nanospheres for removal of methylene blue in water, *Carbon*, 2015, **89**, 378–391.
- 58 H. B. Chen, W. X. Liu and Z. Z. Qin, ZnO/ZnFe<sub>2</sub>O<sub>4</sub> nanocomposite as a broad-spectrum photo-Fenton-like photocatalyst with near-infrared activity, *Catal. Sci. Technol.*, 2017, **7**, 2236–2244.
- 59 F. D. Mai, C. C. Chena, J. L. Chen and S. C. Liu, Photodegradation of methyl green using visible irradiation in ZnO suspensions: Determination of the reaction pathway and identification of intermediates by a high-performance liquid chromatography-photodiode array-electrospray ionization-mass spectrometry method, *J. Chromatogr. A*, 2008, **1189**, 355–365.
- 60 C. Q. Zhang, X. Y. Li, S. Z. Zheng, Y. Y. Ma, *et al.*, Construction of TiO<sub>2</sub> nanobelts-Bi<sub>2</sub>O<sub>4</sub> heterojunction with enhanced visible light photocatalytic activity, *Colloids Surf., A*, 2018, **548**, 150–157.
- 61 Y. W. Jun, J. H. Lee and J. Cheon, Chemical design of nanoparticle probes for high-performance magnetic resonance imaging, *Angew. Chem., Int. Ed.*, 2008, **47**, 5122–5135.

- 62 Y. W. Jun, J. W. Seo and J. Cheon, Nanoscaling laws of magnetic nanoparticles and their applicabilities in biomedical sciences, *Acc. Chem. Res.*, 2008, **41**, 179–189.
- 63 X. H. Li, C. L. Xu, X. H. Han, L. Qiao, T. Wang and F. S. Li, Synthesis and magnetic properties of nearly monodisperse  $\text{CoFe}_2\text{O}_4$  nanoparticles through a simple hydrothermal condition, *Nanoscale Res. Lett.*, 2010, **5**, 1039–1044.
- 64 L. Zou, H. Wang, G. Yuan and X. Wang, Magnetically separable  $\text{CdS/ZnFe}_2\text{O}_4$  composites with highly efficient photocatalytic activity and photostability under visible light, *ACS Appl. Nano Mater.*, 2018, **1**, 831–838.
- 65 Y. He, D. B. Jiang, D. Y. Jiang, J. Chen and Y. X. Zhang, Evaluation of  $\text{MnO}_2$ -templated iron oxide-coated diatomites for their catalytic performance in heterogeneous photo Fenton-like system, *J. Hazard. Mater.*, 2018, **344**, 230–240.
- 66 R. Sharma, S. Bansal and S. Singhal, Tailoring the photo-Fenton activity of spinel ferrites ( $\text{MFe}_2\text{O}_4$ ) by incorporating different cations (M= Cu, Zn, Ni and Co) in the structure, *RSC Adv.*, 2015, **5**, 6006–6018.